ACS APPLIED MATERIALS & INTERFACES

Research Article

Cite This: ACS Appl. Mater. Interfaces 2019, 11, 46714−46725

www.acsami.org

Biohybrid Hydrogel and Aerogel from Self-Assembled Nanocellulose and Nanochitin as a High-Efficiency Adsorbent for Water Purification

Xuefeng Zhang,*[,†] Islam Elsayed,[†] Chanaka Navarathna,[‡] Gregory T. Schueneman,[§] and EI Barbary Hassan*[,†]

[†]Department of Sustainable Bioproducts and [‡]Department of Chemistry, Mississippi State University (MSU), Mississippi State, Mississippi 39762, United States

[§]USDA Forest Service, Forest Products Laboratory, Madison, Wisconsin 53726, United States

Supporting Information

ABSTRACT: A simple and novel method, self-assembly of nanocellulose and nanochitin, was developed to produce high-efficiency and versatile biohybrid hydrogel (BHH) and aerogel (BHA) for water purification. The self-assembly process was driven by the electrostatic force between one-dimensional (1D) negatively charged TEMPO-oxidized cellulose nanofiber (TOCNF) and positively charged partly deacetylated chitin nanofiber (PDChNF). The self-assembly process was performed at room temperature and without adding any cross-linking agents throughout the process. This results in the three-dimensional (3D) BHH that physically cross-linked via both electrostatic interactions and hydrogen bonding between TOCNF and PDChNF. The obtained BHA from lyophilized BHH exhibited a highly porous interconnected structure with a specific surface area of 54 $m^2 \cdot g^{-1}$, which assures the availability of its internal active site for the adsorption of toxic metalloid ions and organic pollutants. Consequently, the BHA displayed super-high adsorption capacities of 217 $mg \cdot g^{-1}$ for As(III) under the neutral pH conditions and 531 $mg \cdot g^{-1}$ for methylene blue (MB) under an alkaline aqueous condition with rapid adsorption kinetics, in sharp contrast to conventional biobased adsorbents. Moreover, the BHA is reusable, which still exhibited a high MB adsorption capacity of 505 $mg \cdot g^{-1}$ even after five successive adsorption−desorption cycles. This versatile BHA produced via a facile preparation strategy is proven to be a promising renewable adsorbent for water purification, offering simple and green alternatives to the conventional adsorbent from synthetic polymers.

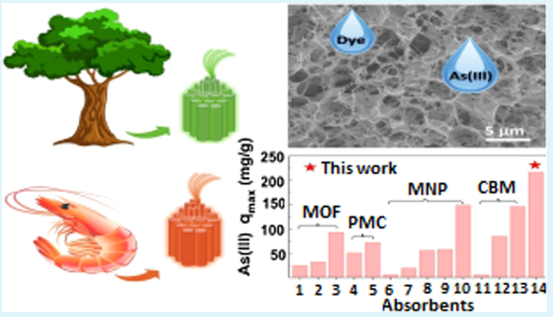

KEYWORDS: *nanocellulose, nanochitin, self-assembled hydrogel, aerogel, arsenite [As(III)] absorption*

1. INTRODUCTION

Toxic metals and metalloids and deleterious organic contaminents are water pollutants worldwide that cause severe water safety problems. Arsenic poisoning has been recognized in many countries and is a global health problem that threatens more than 150 million people worldwide.[1] Arsenic is a metalloid that forms highly toxic compounds in many oxidation states including arsenite [As(III)] and arsenate [As(V)]. As(III) is reported to be more toxic than As(V) and more difficult to remove from water.[2] Although ion-exchange, membrane filtration, coagulation, reaction with metal salts and lime followed by filtration and adsorption are widely used for arsenic-contaminated water remediation, current techniques are not always efficient, as they suffer from poor sorption capacities. Due to the harmful effects of dyes, the US Environmental Protection Agency is instructing industries to eliminate dyes from effluents. Excessive levels of dyes in discharge water can destroy aquatic organisms because their toxic, carcinogenic, and negative effects on the photosynthetic activity of aquatic plants and microorganisms.[3] Methylene blue (MB) is a cationic thiazine dye being widely used in different fields including textile, biology, chemistry, and medicine. Because of its low toxicity and well-known adsorption characteristics, MB has been used as a model compound for investigating the sorption of dye.[4] Although synthetic polymeric resins have been reported for the sorptive removal of MB with high adsorption capacity,[5] the use of synthetic polymers can be a concern due to their inherent non-renewability and low biodegradability.

Aerogels are a porous material with a high surface area that have been widely used as sorbents for water purification.[6−8] Natural-polymer-derived aerogels have drawn a lot of attention because of their biodegradability and biocompatibility. In recent years, cellulose and chitin, two of the most abundant

Received: August 22, 2019
Accepted: November 19, 2019
Published: November 19, 2019

DOI: 10.1021/acsami.9b15139
ACS Appl. Mater. Interfaces 2019, 11, 46714−46725

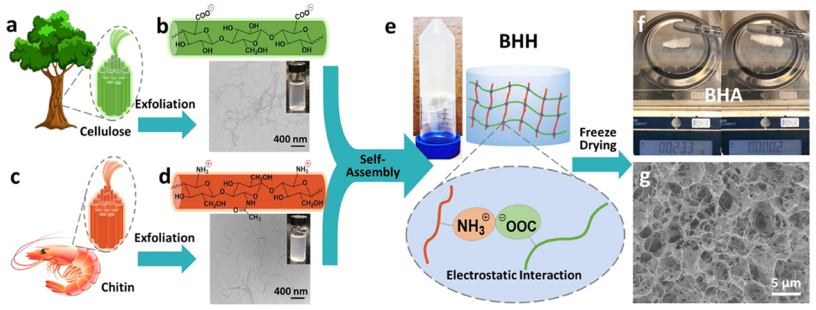

Figure 1. Schematic of the self-assembly process for the production of BHH and BHA. (a, b) TEMPO and mechanical exfoliation to produce TOCNF; (c, d) NaOH and mechanical exfoliation to produce PDChNF; (e) electrostatic-force-induced self-assembly gelation of nanofibers with ionic interactions between TOCNF and PDChNF; (f) digital images illustrate that the ultralight BHA was captured by a marker pen due to static electricity; and (g) scanning electron microscopy (SEM) image of BHA exhibits a highly porous structure.

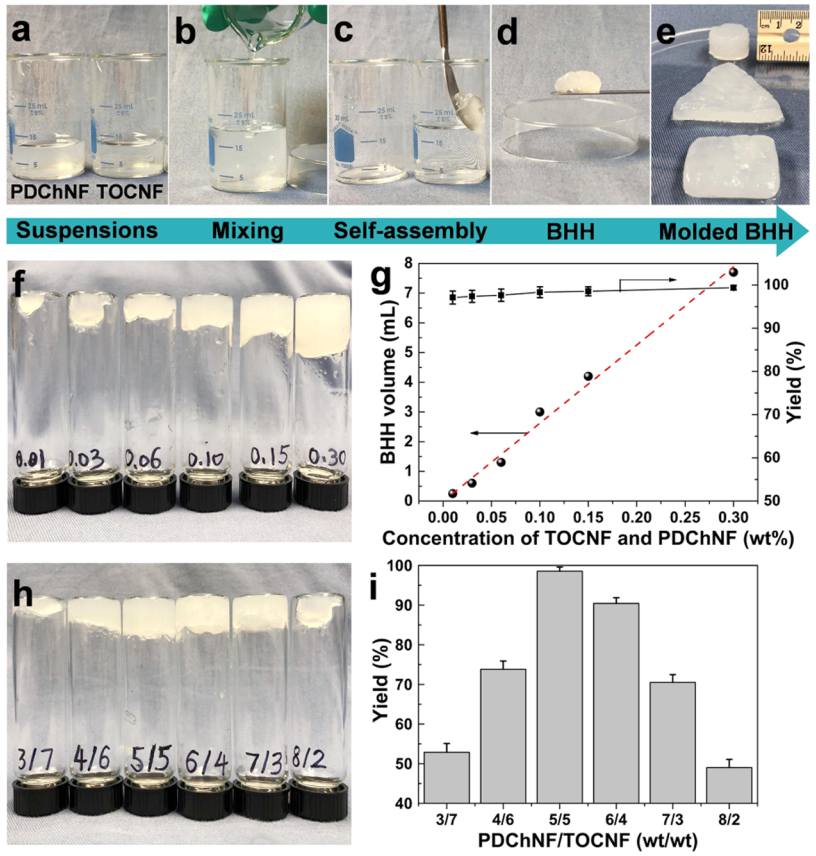

Figure 2. Digital image of (a) TOCNF (0.03 wt %) and PDChNF (0.03 wt %) suspensions; (b) mixing of TOCNF and PDChNF suspensions; (c) BHH formed through the self-assembling of TOCNFs and PDChNF and expelling of water; (d) freestanding BHH; (e) different shapes of BHHs produced through molding; (f) BHHs produced from different initial concentrations of nanofibers (PDChNF/TOCNF = 5/5 in weight); (g) BHH volume and self-assembly yield as a function of the initial concentration of nanofibers; (h) BHHs produced from different PDChNF/TOCNF mass ratios (initial concentration of nanofibers = 0.15 wt %); and (i) self-assembly yield as a function of PDChNF/TOCNF mass ratio.

biopolymers in the biosphere, have been used for the production of aerogels.[8−12] Generally, cellulose- or chitin-based aerogels are produced through sublimating water from their corresponding hydrogels. Although hydrogels can be prepared from native cellulose or chitin through dissolution and gelation processes, only a few solvents have been discovered to be effective in dissolving cellulose and chitin,[13] thus limiting their potential. Alternatively, hydrogels can be prepared from nanocellulose or nanochitin aqueous suspensions. With the aid of chemical cross-linkers, either etherifying or esterifying reagents, a variety of chemically cross-linked hydrogels were produced.[10,14] Despite their good mechanical properties, the use of hazardous chemicals decreases their environmental compatibility. Physically cross-linked hydrogels can also be prepared from nanocellulose or nanochitin because of their high aspect ratio and abundant surface functional groups. However, special conditions including ultrasonication, pH adjustment, thermal initiation, and solvent exchange are required to initiate gelation through physical entanglements, hydrogen bonds, or ionic interactions.[15−17] Therefore, the exploration of simple processes for the production of physical hydrogels from nanocellulose or nanochitin is a priority.

To date, limited studies have been reported to produce biohybrid hydrogels (BHHs) and aerogels (BHAs) from

DOI: 10.1021/acsami.9b15139
ACS Appl. Mater. Interfaces 2019, 11, 46714−46725

cellulose and chitin. Previously, BHH beads and films were obtained through solvent exchange with deionized water after dissolution in ionic liquid or NaOH/thiourea solvent.[18−23] After water removal, the porous biohybrid beads and films showed good sorption performance for the removal of heavy metals from aqueous solutions. Until now, only Gao et al. have reported physical BHHs synthesized from chitin/cellulose nanofibers after (2,2,6,6-tetramethylpiperidine-1-oxylradical)-mediated oxidation (TEMPO oxidation), resulting in BHAs with a specific surface area of up to 94 $m^2 \cdot g^{-1}$.[24] However, in this study, the gelation of chitin/cellulose nanofibers was induced via a time-consuming pH adjustment process with acid. Moreover, a tedious solvent exchange process was required to remove acid after hydrogel formation, which makes the process less appealing. Furthermore, no applications have been reported for this BHA.

Herein, we explored the production of BHHs through a facile electrostatic-force-induced self-assembly gelation process with nanocellulose and nanochitin (Figure 1). TEMPO-oxidized cellulose nanofiber (TOCNF) with negatively charged surface and partly deacetylated chitin nanofiber (PDChNF) with positively charged surface was prepared through TEMPO-oxidation and alkaline solution treatment, respectively.[10,25] The gelation behavior was investigated using different concentrations and combinations of TOCNF and PDChNF. Additionally, the BHH produced at the optimized condition was freeze-dried to obtain the BHA, which was characterized using infrared and X-ray spectroscopies to investigate the interactions between TOCNF and PDChNF. Furthermore, the adsorption of As(III) and MB onto BHA was examined and found to exhibit super-high As(III) (217 $mg \cdot g^{-1}$) and methylene blue (531 $mg \cdot g^{-1}$) adsorption capacities. Such adsorption capacities are higher than any previously reported all-biobased polymer adsorbents. This work is of great significance, because we not only provide a simple and novel method for the production of cellulose- and chitin-based hydrogel and aerogel, but also demonstrate a high-efficiency biobased superadsorbent for water purification.

2. RESULT AND DISCUSSION

2.1. BHH from Self-Assembly of TOCNF and PDChNF.

In the present work, nanocellulose- and nanochitin-based BHH and BHA were produced via a facile electrostatic-force-induced self-assembly gelation process employing negatively charged TOCNF and positively charged PDChNF. Figure 1 illustrates a general description of the self-assembly process. Through TEMPO oxidation and mechanical defibrillation, TOCNF could achieve a surface carboxylate (COO^-) content of 1.43 $mmol \cdot g^{-1}$ (Figure S1a, Supporting Information), and an aspect ratio of up to 1000 (Figure 1b). The high anionic electrostatic repulsions of COO^- groups endowed very stable and homogeneous TOCNF aqueous colloidal suspensions at pH ∼ 6 (Figure S1b) that exhibit the characteristic shear-thinning behavior (Figure S1c). Through alkaline treatment (33 wt % NaOH at 90 °C for 3.5 h) and mechanical defibrillation, PDChNF could achieve a surface primary amino ($-NH_2$) content of 2.10 $mmol \cdot g^{-1}$ (corresponding to the removal of 39% surface acetyl groups; Figure S1d) and an aspect ratio of up to 500 (Figure 1d). The high cation electrostatic repulsions of protonated $-NH_2$ ($-NH_3^+$) groups at pH ∼ 5.6 ensured very stable and homogeneous PDChNF aqueous colloidal suspensions (Figure S1e) that exhibit the characteristic shear-thinning behavior (Figure S1f).

When mixing the aqueous colloidal suspensions of TOCNF and PDChNF, the self-assembly of a three-dimensional (3D) network commences immediately because of the strong electrostatic attraction between NH_3^+ and COO^- groups on the nanofibers (Figure 2a,b). Slightly shaking the mixture for 20 s accelerates the self-assembly of nanofiber (3D) network (Video S1). When excess water is expelled from the 3D network by the centrifugal force generated from shaking (Video S1), TOCNF and PDChNF self-assemble to a more compact structure and form an opaque BHH (Figure 2c,d). The opaque BHH is expected as the self-assembly results in the gelation of nanofibers and phase separation, which results in a heterogeneous distribution of nanofibers in BHA.[13] The freshly prepared BHH can be molded into different shapes, as shown in Figure 2e.

Further investigation suggests that the formation of BHH was a concentration-independent process. As shown in Figure 2f, when the initial concentrations of the PDChNF and TOCNF suspensions increased from 0.01 to 0.30 wt %, the volume of the as-synthesized BHH increased from approximately 0.25−7.7 mL, at high linearity with an R^2 of 0.99 (Figure 2g). In other words, at higher concentrations, the self-assembled nanofiber 3D networks are able to hold more water and result in BHHs with large volumes, because of the suspensions containing more nanofibers. After freeze-drying of frozen BHHs, the BHAs were obtained and their weights were measured to calculate the self-assembly yield use by the following equation

$$\text{yield}\ (\%) = W_{\text{BHA}}/(W_{\text{TOCNF}} + W_{\text{PDChNF}}) \times 100\% \qquad (1)$$

where W_{BHA}, W_{TOCNF}, and W_{PDChNF} are the dry weights of BHA, TOCNF, and PDChNF, respectively. As shown in Figure 2g and Table S1 in SI, the self-assembly yields maintain a constant value of 98 ± 1% for all tested concentrations. This result confirms that the self-assembly was a concentration-independent process.

To further understand the self-assembly process, we investigated the effect of PDChNF/TOCNF mass ratio on the formation of BHH. Keeping the total amount of PDChNF and TOCNF constant, the volume of resultant BHHs varies with the change of PDChNF/TOCNF mass ratio (Figure 2h). The dried weights of BHHs were then measured to calculate the self-assembly yields. As shown in Figure 2i and Table S1 in SI, the self-assembly yield initially increased with increasing PDChNF/TOCNF mass ratio, with a maximum of 99%, occurring at the PDChNF/TOCNF mass ratios of 5/5. Over 6/4, however, the yield drops to 49% at 8/2 of PDChNF/TOCNF mass ratio. These results clearly indicate that self-assembly is a mass-dependent process. At the PDChNF/TOCNF mass ratio of 5/5, nearly all of the nanofibers are participating in self-assembly and formed the BHH with the highest yield. Thus, the optimized mass ratio of PDChNF/TOCNF for BHH production is 5/5. As mentioned before, the self-assembly of PDChNF and TOCNF was driven by the electrostatic attraction between $-COO^-$ and $-NH_3^+$ in nanofibers. The amount of surface $-COO^-$ in TOCNFs is 1.43 $mmol \cdot g^{-1}$, whereas the amount of surface $-NH_3^+$ in PDChNF is 2.10 $mmol \cdot g^{-1}$. When mixing PDChNF and TOCNF at a mass ratio of 5/5 to achieve the maximum self-assembly yield, the net charge from PDChNF and TOCNF was not equal to zero. This is a quite interesting observation, suggesting that the higher charge of the PDChNF is required to maintain the gelation of the nanofiber suspensions, and this

DOI: 10.1021/acsami.9b15139
ACS Appl. Mater. Interfaces 2019, 11, 46714−46725

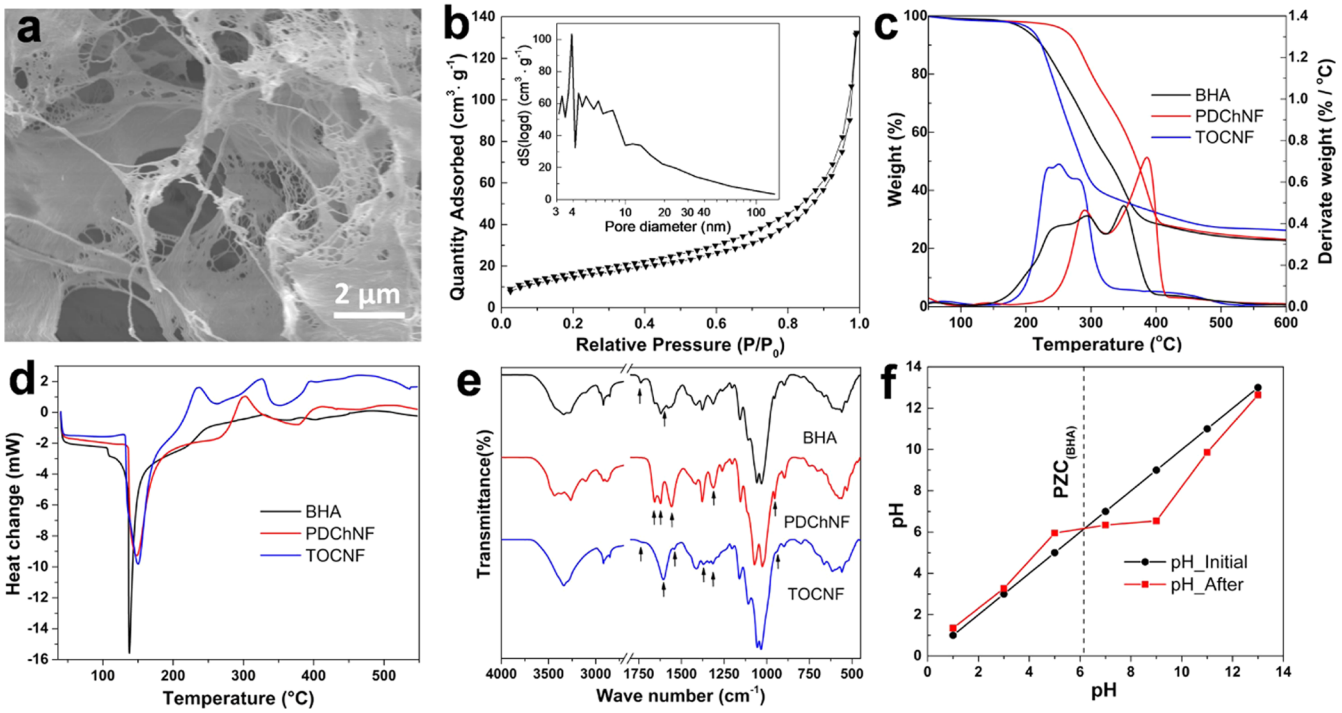

Figure 3. (a) SEM images of BHA show a porous cell structure with a film-like or net-like cell morphology; (b) N_2 adsorption/desorption isotherm and pore size distribution (inserted image) of BHA; (c) thermogravimetric analysis (TGA) and derivative thermogravimetric (DTG) curves of BHA, PDChNF, and TOCNF; (d) differential scanning calorimetric (DSC) curves of BHA, PDChNF, and TOCNF; (e) Fourier transform infrared (FTIR) spectra of BHA, PDChNF, and TOCNF; and (f) point of zero charge PZC determination curve of BHA.

could be attributed to the fact that the dimension and aspect ratio of TOCNF are large than those of PDChNF.

The greatest advantage of this "self-assembly" was avoiding the use of hazardous chemical cross-linkers and acidic/alkaline solutions. Moreover, owing to the strong electrostatic attraction between PDChNF and TOCNF, the self-assembly is a super quick process that is completed within 1 min (Video S1, Supporting Information), which is far less than any previously reported physical and chemical cross-linked nanocellulose- and nanochitin-based hydrogels, and those preparation processes usually require several hours to several days.[10,12,24] In addition to green and time efficiency, this method is very easy to apply, and the self-assembled BHH could be prepared with a very low concentration (0.01 wt %, Figure 2f) of PDChNF and TOCNF, in sharp contrast to the conventional methods that a minimum nanofiber concentration of at least 0.2 wt % is required.[10,12,24,26]

2.2. Characterization of BHA. The BHH synthesized at the optimized conditions (PDChNF/TOCNF = 5/5 in weight) was used to produce BHA through a lyophilization process. The obtained BHA was characterized and used for water purification.

2.2.1. Density and Porosity. After freeze-drying of frozen BHH, ultralight and high porosity BHA was obtained, which can be easily attracted by electrostatic force (Figure 1f). The density of aerogels prepared from the PDChNF/TOCNF mass ratios of 5/5 is 8.2 ± 0.9 mg·cm^{-3}, and the corresponding porosity is 99.44 ± 0.07%; changing the initial concentration of TOCNF and PDChNF suspensions does not affect the BHA's density or porosity. The self-assembled BHA was fragile and collapsed when handling with tweezers (Figure S2). This weak mechanical response was expected due to the absence of chemical cross-linking reagents during hydrogel preparation. The BHA exhibits a highly porous structure that contains heterogeneously shaped cells ranging in size from 2 to 10 μm and wrapped in thin walls with many fibrils (Figure 1g). The cell walls exhibit either a film-like or a net-like structure, and the pore diameter of the "net" is usually less than 100 nm (Figure 3a). This phenomenon was attributed to the phase separation of nanofibers during the self-assembly process, in which the nanofiber-rich phase formed film-like cell walls, while the nanofiber-poor phase formed net-like cell walls. Although the net-like cell walls diminished the mechanical strength of BHA, this porous structure is important for applying BHA as an adsorbent for water purification. The BHA exhibits a type IVa N_2 adsorption/desorption isotherm with a type H3 hysteresis loop (Figure 3b), indicating the existence of both mesopores and macropores. These mesopores and macropores are mainly present on the BHAs' net-like cell walls, as shown in the SEM image (Figure 3a). The Brunauer–Emmett–Teller (BET) surface area of BHA was 54 m^2·g^{-1}, and the total pore volume was 0.194 cm^3·g^{-1}, which are comparable to the previously reported nanocellulose and nanochitin aerogels.[10,12,24] Moreover, this hierarchical mesoporous–macroporous structure is advantageous because the macropores enable faster molecular diffusion and mass transfer (especially for large molecules) and the mesopores provide more active sites for adsorption during water purification.

2.2.2. Thermal Properties. The thermal stability of TOCNF, PDChNF, and BHA was tested by thermogravimetric analysis (TGA) (Figure 3c). The derivative thermogravimetric (DTG) curve of TOCNF shows a peak centered at 251 °C with two shoulder peaks located at 236 and 278 °C, respectively. The DTG curve of PDChNF exhibits two peaks centered at 290 and 385 °C, respectively. The BHA shows three main DTG peaks located at 257, 294, and 351 °C,

DOI: 10.1021/acsami.9b15139
ACS Appl. Mater. Interfaces 2019, 11, 46714–46725

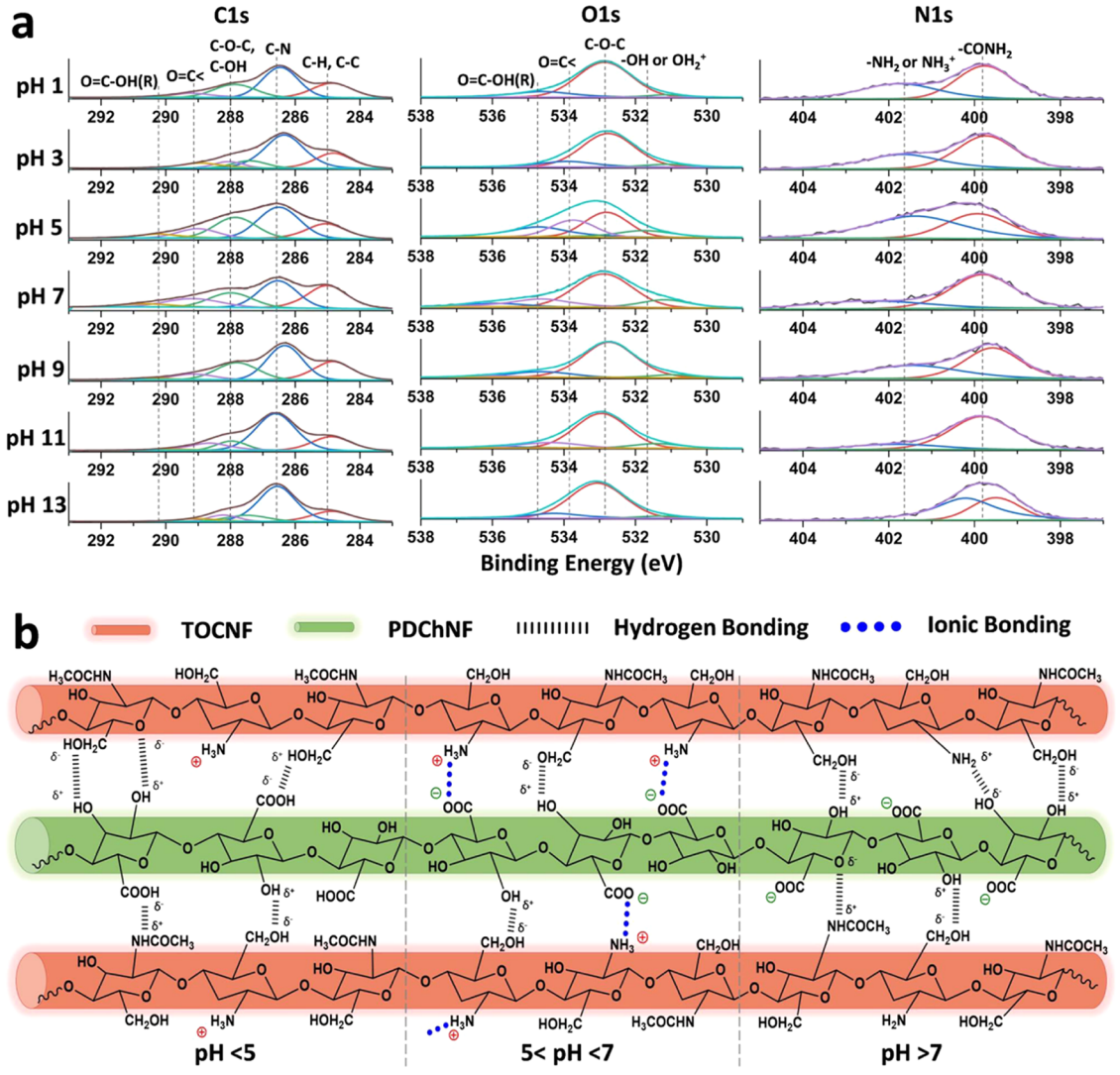

Figure 4. (a) XPS spectra of C 1s, O 1s, and N 1s for BHA at different initial solution pH values; and (b) proposed pH-dependent intermolecular interactions between TOCNF and PDChNF in BHA.

respectively. The first peak can be attributed to the thermal degradation of TOCNF, the second peak corresponds to the decomposition of both TOCNF and PDChNF, and the third peak was mainly attributed to the thermal degradation of PDChNF. However, the third peak has a much lower temperature in comparison with that of chitin, indicating that the BHA has a loose and porous structure, thus easily being decomposed. The differential scanning calorimetric (DSC) graphs for TOCNF, PDChNF, and BHA shows an exotherm at 140−155 °C, which corresponds to the moisture loss (Figure 3d). The TOCNF loses its mass in two stages at 215−250 and 310−400 °C, which could be attributed to the corresponding carboxylate group decomposition and the degradation of unmodified crystalline cores, respectively.[27] The PDChNF shows an endotherm in 290−310 °C, possibly due to the decomposition of amine and amide groups.[28] BHA shows a significantly low heat flow in 200−400 °C range, which could be due to the presence of more protonated and hydrogen-bonded structures.[27]

2.2.3. Fourier Transform Infrared (FTIR) Spectroscopy. To explore the interactions between TOCNF and PDChNF, the FTIR spectra of lyophilized TOCNF, PDChNF, and BHA were recorded (Figure 3e). The spectrum of PDChNF shows the characteristic doublet amide I bonds (1622 and 1648 cm^{-1}) and the amide II band at 1557 cm^{-1}. Fingerprint peaks, C−O stretch at 1312 cm^{-1}, and out-of-plane OH bending 955 cm^{-1} were also observed. The spectrum of TOCNF exhibits a sharp and large carboxylate ($-COO^-$) peak at 1606 cm^{-1} and a small shoulder carboxylic acid (−COOH) peak at 1737 cm^{-1}.[29] Additionally, asymmetric $-COO^-$ stretching band at 1542 cm^{-1} and symmetric $-COO^-$ stretch band at 1371 cm^{-1} were also observed. Peaks at 1316 and 941 cm^{-1} are for OH bending (out of plane) and C−O stretching, respectively. The spectrum of BHA displays characteristic bands of both PDChNF and TOCNF; however, peak shifting and intensity changing were observed on these bands. Specifically, the spectrum of BHA shows a higher peak at 1737 cm^{-1} (−COOH) and a lower peak at 1606 cm^{-1} ($-COO^-$) in comparison with that of TOCNF. Moreover, the spectrum of BHA exhibits lower absorption intensities of both amide I- and amide II-related bands in comparison with that of PDChNF (Figure S3). Furthermore, the N−H and O−H stretching absorption bands of BHA were shifted from 3263 to 3281 cm^{-1} and from 3438 to 3428 cm^{-1} (Figure S3). These findings confirmed that the self-assembly gelation of TOCNFs and PDChNF was driven by electrostatic interaction between

DOI: 10.1021/acsami.9b15139
ACS Appl. Mater. Interfaces 2019, 11, 46714−46725

Table 1. XPS Data for BHA at Different Initial Solution pH Levels[a]

peak			pH 1	pH 3	pH 5	pH 7	pH 9	pH 11	pH 13
C 1s	(R/H)O−C═O	BE (eV)[a]	290.0	288.9	290.2	290.6	290.5	289.6	289.0
		atomic %	0.6	5.5	3.4	3.2	1.5	1.2	3.0
		FWHM (eV)	1.5	1.5	1.5	2.0	1.5	1.5	1.5
	O═C<	BE (eV)	289.2	288.1	289.0	289.2	289.1	288.7	288.2
		atomic %	4.8	4.5	6.7	8.9	4.7	7.4	4.6
		FWHM (eV)	1.5	1.1	1.5	2.0	1.5	1.5	1.1
	C−O−C	BE (eV)	287.9	287.4	287.9	288.0	287.8	288.0	287.5
		atomic %	13.4	5.8	16.1	11.8	14.6	6.0	6.2
		FWHM (eV)	1.5	1.2	1.5	1.6	1.5	1.1	1.5
	C−N	BE (eV)	286.5	286.3	286.5	286.5	286.3	286.6	286.6
		atomic %	26.6	31.9	24.0	19.4	25.1	31.5	33.3
		FWHM (eV)	1.3	1.4	1.5	1.4	1.3	1.4	1.4
	C−H, C−C	BE (eV)	284.9	284.8	285.1	285.0	284.8	284.9	284.9
		atomic %	14.5	13.6	11.4	18.0	15.3	12.1	10.4
		FWHM (eV)	1.4	1.3	1.4	1.5	1.4	1.4	1.4
O 1s	(R/H)O−C═O	BE (eV)			534.7	536.0	536.0	536.0	
		atomic %			8.0	2.4	1.3	1.3	
		FWHM (eV)			2.0	2.0	2.0	1.9	
	O═C<	BE (eV)	534.6	533.9	533.7	534.6	534.6	534.4	534.3
		atomic %	5.7	5.3	8.9	6.5	4.8	5.0	5.4
		FWHM (eV)	1.9	1.9	1.5	2.0	2.0	2.0	1.8
	C−O−C	BE (eV)	532.9	532.8	532.8	532.9	532.7	533.0	533.1
		atomic %	29.6	27.7	13.1	22.4	27.5	28.8	33.2
		FWHM (eV)	1.8	1.7	1.5	1.9	1.7	1.7	1.8
	−OH or OH_2^+	BE (eV)	531.4	531.1	531.8	531.2	531.0	531.4	531.3
		atomic %	1.9	2.4	5.0	5.0	2.2	3.9	2.2
		FWHM (eV)	1.3	1.6	1.9	1.6	1.4	1.6	1.6
N 1s	$-NH_2$, $C-NH^+$, NH_3^+	BE (eV)	401.8	401.7	401.4	402.5	401.5	401.8	400.4
		atomic %	1.1	1.3	2.0	0.7	1.3	0.5	0.7
		FWHM (eV)	2.1	2.1	2.6	3.2	2.6	2.5	2.2
	−CONH	BE (eV)	399.8	399.7	399.9	399.8	399.6	399.8	399.7
		atomic %	1.7	2.0	1.4	1.8	1.7	2.3	1.1
		FWHM (eV)	1.5	1.6	1.7	1.7	1.5	1.7	1.6

[a]The BE values were estimated with a maximum error of ±0.05 eV in curve fitting.

$-COO^-$ and $-NH_3^+$ groups. In addition, these findings also indicate that strong hydrogen-bonding interactions were formed between TOCNFs and PDChNF in BHH and BHA.

2.2.4. Point of Zero Charge (PZC). The PZC is an important index that provides the surface charge information and explains many sorption-related phenomena of materials. As shown in Figure 3f, BHA exhibits different charge behaviors at different pH levels. Specifically, at a solution pH lower than 6.16, the surface of BHA was positively charged, which is attributed to the predominant influence of $-NH_3^+$ from PDChNF. At a solution pH higher than 6.16, the surface of BHA was negatively charged, and this can be attributed to the predominant effect of $-COO^-$ from TOCNF. Thus, the PZC of BHA [$PZC_{(BHA)}$] appears at the pH of 6.16. It is worth to note that the pK_a of $-NH_2$ and −COOH groups are 6.5, and 4.8, respectively.[30] Therefore, this PZC value is expected because the BHA's surface $-COO^-$ and NH_3^+ groups are equal to zero at pH 6.16 through stoichiometric calculations (shown in SI).

2.2.5. X-ray Photoelectron Spectroscopy (XPS). According to the PZC, at the pH range of 4.8−6.5, the $-NH_3^+$ and $-COO^-$ are predominant groups onto BHA. The negatively charged $-COO^-$ groups could interact with $-NH_3^+$ within the steric hindrance, flexibility, and proximity limits to form an ionic network-like structure. To confirm the ionic interactions between $-NH_3^+$ and $-COO^-$ groups, XPS experiments were conducted. BHA samples were equilibrated in NaCl solution with different pH values, followed by vacuum drying as preparation prior to XPS analysis. Figure 4 shows the XPS of BHA, which probed the chemical states of C, O, and N as a function of equilibration pH. In general, the C 1s, O 1s, and N 1s spectra can be resolved into five, four, and two peaks, respectively. The binding energies (BE), atomic percentages, and peaks' full width at half-maximum (FWHM) of those resolved peaks are presented in Table 1. Specifically, the highest binding energy (290.6−288.9 eV) peak in C 1s is corresponding to −COOH(R) oxidation states. Peaks in 289.2−288.2 eV range belong to keto (>C═O) carbons but overlap with −COOH(R) and C−OH, C−O−C regions (288.0−287.4 eV), making these evaluations approximate. Peaks in the range 286.6−286.3 and 285.1−284.8 eV are for C−N and C−H, and C−C, respectively. Peaks were resolved in the O 1s XPS binding energy (BE) ranges of 536.0−534.7, 534.6−533.7, 533.1−532.7, and 531.8−531.0 eV. These regions are assigned to O−C═O(R), O═C<, −C−O−C, and OH or OH_2^+, respectively. The N 1s curve-resolved envelop was interpreted for $-NH_2$ or NH_3^+ 401.8−400.4 eV and −CONH 399.9−399.6 eV on PDChNF.

The pseudo-zwitterionic state of BHA at its $PZC_{(BHA)}$ (6.16) was confirmed by XPS. At the pH level of 7 (close to the

DOI: 10.1021/acsami.9b15139
ACS Appl. Mater. Interfaces 2019, 11, 46714−46725

$PZC_{(BHA)}$), the binding energies of the functional groups that are responsible for ionic interactions reach their maximum values (Table 1). For instance, at pH 7, the BEs of C 1s and O 1s for O═C−O(R) reached their maximum of 290.6 and 536.0 eV, respectively; the N 1s ($-NH_2$, $C-NH^+$, $-NH_3^+$) peaks reached their maximum of 402.5 eV. This observation clearly indicates the presence of a complex chemical environment for XPS electron ejection, i.e., strong ionic interaction between $-NH_3^+$ and $-COO^-$ groups onto BHA. As the pH levels were greater than 7, the XPS BEs of $-NH_3^+$ shifted to a much lower BE region (up to 400.4 eV at pH 13; Table 1); this indicated a decline of ionic interaction and can be attributed to the decrease of protonation degree of $-NH_3^+$. On the other hand, as the pH levels lower than 7, the XPS BEs of O 1s for O═C−O(R) shifted to a lower BE region of 534.7 eV at pH 5 (Table 1) and further become invisible at much lower pH levels (1 and 3). This phenomenon also indicated a decline of ionic interaction as the decrease of pH from 7 to 1, and which was related to the increasing protonation degree of $-COO^-$. Thus, the interactions between TOCNF and PDChNF in BHA were governed primarily by the ionic interaction at the pH range 5−7. This observation also confirmed that the self-assembly of TOCNF and PDChNF was driven by the electrostatic force from ionic interaction due to the self-assembly being conducted at pH ∼ 6. Moreover, at the pH levels below 5 and above 7, it can be concluded that the interactions between TOCNF and PDChNF in BHA were primarily governed by hydrogen bonding. Overall, based on the evidence from FTIR, PZC, and XPS, the following pH-dependent interactions were proposed for TOCNF and PDChNF in BHA (Figure 4b).

2.3. MB and Arsenic Adsorptions. *2.3.1. Effect of Initial pH.* MB is a cationic dye (unprotonated, MB^+) in a wide pH range (pH 0−14); it can exist as mono (HMB^{2+})- or diprotonated (H_2MB^{3+}) forms at acidic pH conditions due to the protonation of its nitrogen groups (terminal and ring).[31] At basic pH conditions, unprotonated MB can still carry a positive charge (MB^+) on its sulfur atom. The positive charge on the sulfur atom can delocalize to the terminal nitrogen atom that can be electrostatically attracted by the negatively charged functional groups. Figure 5a illustrates the removal of MB by BHH and BHA from neutral MB aqueous solution. The adsorption of MB onto BHA is pH-dependent, as shown in Figure 5b; the adsorption capacity (q_e) significantly increased from 2.4 to 303 $mg{\cdot}g^{-1}$ with the increasing initial MB solution pH from 2 to 10. This pH dependence is expected due to MB being an ionic dye with a positive charge, and BHA exhibits different charge behaviors at different pH levels as mentioned before. Generally, at a solution pH lower than 6.16, the BHA exhibits a positive net surface charge (Figure 3f), which is unfavorable for MB adsorption because of the electrostatic repulsion. On the other hand, the BHA exhibits a positive net surface charge at the solution pH levels higher than 6.16, thereby being favorable for MB removal because of the electrostatic attraction. It is worth to note that at pH 4, the BHA still shows a good MB removal efficiency with an adsorption capacity of 51 $mg{\cdot}g^{-1}$. This phenomenon reveals that in addition to these electrostatic interactions, the hydrogen bonds between BHA and MB were also playing an important role for MB adsorption.

Figure 5c displays the arsenite speciation versus pH and pH dependency of As(III) sorption onto BHA. H_3AsO_3 predominates in solution through pH 9, and $H_2AsO_3^-$ begins to form

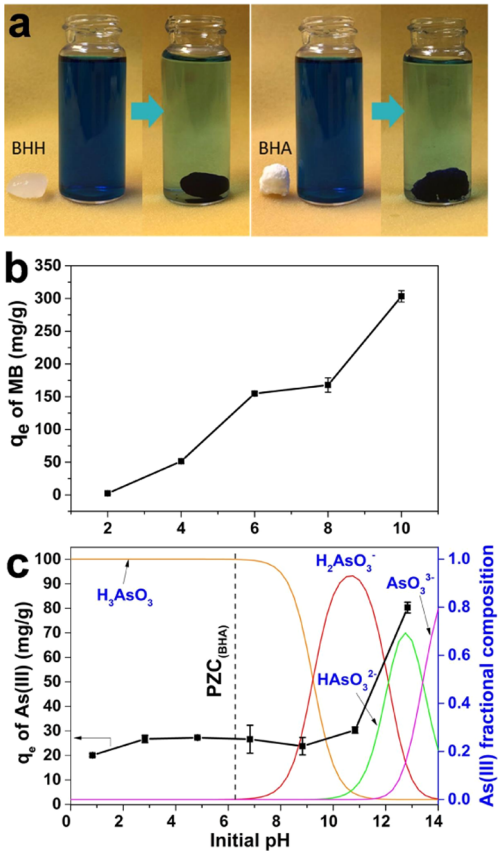

Figure 5. (a) Digital image of MB absorption by BHH and BHA (C_0 = 50 $mg{\cdot}L^{-1}$, t = 24 h, T = 25 °C), and (b, c) effect of initial pH on the adsorption of (b) MB (C_0 = 50 $mg{\cdot}L^{-1}$, t = 24 h, T = 25 °C) and (c) As(III) (C_0 = 10 $mg{\cdot}L^{-1}$, t = 2 h, T = 25 °C).

at pH around 8 and predominates from a pH range of 9.2 to 12. $HAsO_3^{2-}$ is first formed at pH around 10 and is the dominant species from a pH range of 12.2 to 13. Additionally, H_3AsO_3 can be protonated ($H_4AsO_3^+$, not shown in Figure 5b) but only in strongly acidic solutions (i.e., at pH < ∼1.5). Thus, at the solution pH of 1, H_3AsO_3 and $H_4AsO_3^+$ are the main As(III) species being adsorbed. Although the electrostatic repulsion between $-NH^{3+}$ and $H_4AsO_3^+$ may reduce As(III) uptake somewhat, the adsorption at pH of 1 remains robust (20 $mg{\cdot}g^{-1}$). At the solution pH between 2 and 7, H_3AsO_3 is the only As(III) species being adsorbed with an adsorption capacity of around 26 $mg{\cdot}g^{-1}$, and the adsorption be attributed to the hydrogen bonding between H_3AsO_3 and BHA surface functional groups (i.e., $-NH_2$ and −OH).[32] At the solution pH ranges from 7 to 9, H_3AsO_3 is gradually deprotonated to $H_2AsO_3^-$, while the adsorption capacity remains unchanged. A further increase in solution pH from 9 to 13 leads to the formation of $HAsO_3^{2-}$ and AsO_3^{3-} and the rise of adsorption capacity up to 80 $mg{\cdot}g^{-1}$ at a solution pH of 13. The significantly improved adsorption capacity at pH 13 could be attributed to the complete dissociation of H_3AsO_3 to $H_xAsO_3^{y-}$, which may facilitate the formation of hydrogen bonding. Additionally, under strongly alkaline conditions, the interchain interactions between TOCNF and PDChNF in BHA may become loose under a strong alkaline condition (i.e., pH of 12), thereby making more surface functional groups available for arsenite uptake through hydrogen bonds. Although the electrostatic repulsion between $-COO^-$ and

DOI: 10.1021/acsami.9b15139
ACS Appl. Mater. Interfaces 2019, 11, 46714−46725

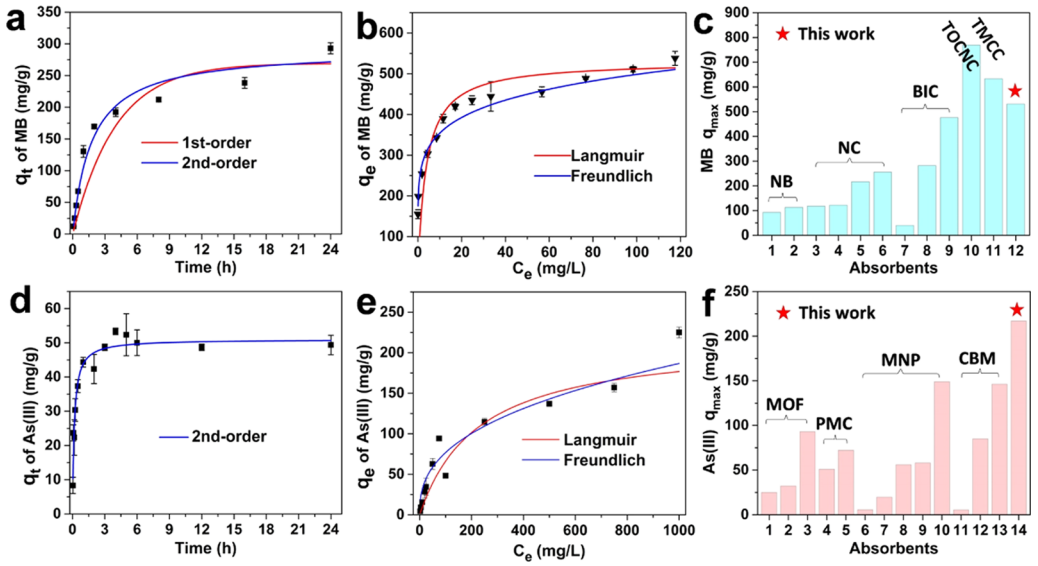

Figure 6. (a) Kinetic models for MB adsorption (pH=10, C_0 = 50 mg·L^{-1}, T = 25 °C); (b) isothermal models for MB adsorption (pH=10, t = 24 h, T = 25 °C); (c) comparison of maximum MB adsorption capacity (q_{max}) of BHA with other materials (detailed in Table S2); (d) kinetic models for As(III) adsorption (pH = 7, C_0 = 200 mg·L^{-1}, T = 25 °C); (e) isothermal models for As(III) adsorption (pH = 7, t = 2 h, T = 25 °C); and (f) comparison of As(III) q_{max} of BHA with other materials (detailed in Table S3).

$H_xAsO_3^{x-}$ may reduce As(III) uptake somewhat under strongly alkaline conditions, the adsorption through hydrogen bonding remains robust (up to 80 mg·g^{-1}). Therefore, over the entire pH range of 1−13, BHA remains an effective As(III) adsorbent.

2.3.2. Adsorption Kinetics and Isotherms. Figure 6a shows the adsorption kinetics of MB onto BHA. It is clear that the adsorption of MB increased rapidly in the first 3 h, and the removal of MB reached the adsorption equilibrium within 12 h (Figure 6a). The data were fitted to both pseudo-first-order (first-order, eq 2) and pseudo-second-order (second-order, eq 3) models well (Table 2)

$$\ln(q_e - q_t) = \ln q_e - k_1 t \quad (2)$$

$$\frac{t}{q_t} = \frac{1}{k_2 q_e^2} + \frac{t}{q_e} \quad (3)$$

Table 2. Kinetic and Isothermal Parameters for MB and As(III) Adsorptions onto BHA

		adsorbate	
model	parameters	MB	As
first-order kinetic	k_1 (g·mg^{-1}·h^{-1})	0.2516	N/A
	q_{exp} (mg·g^{-1})	293	
	q_{cal} (mg·g^{-1})	269.33	
	R^2	0.99	
second-order kinetic	k_2 (g·mg^{-1}·h^{-1})	0.0019	0.1192
	q_{exp} (mg·g^{-1})	293	49.33
	q_{cal} (mg·g^{-1})	291.54	50.98
	R^2	0.99	0.95
Langmuir isotherm	K_L (L·g^{-1})	0.27055	0.00438
	q_0 (mg·g^{-1})	530.76	217.00
	R^2	0.99	0.99
Freundlich isotherm	K_F	251.67	12.96
	n	6.73	2.58
	R^2	0.99	0.99

where t is the contact time (h), q_e is the adsorbed concentration of MB or As(III) (mg·g^{-1}) at equilibrium, q_t is the equilibrium concentration of MB or As(III) (mg·g^{-1}) at time t, and k_1 and k_2 are the rate constants (g·mg^{-1}·h^{-1}).

Figure 6b shows the adsorption isotherms of MB onto BHA. The adsorption isotherm data were fitted well for both Langmuir and Freundlich models (Table 2). Langmuir isotherm assumes a homogeneous surface, monolayer coverage, and no interactions of the adsorbate with neighboring sites, and Freundlich isotherm is used in the low-to-intermediate adsorbate concentration range.[33] The maximum Langmuir adsorption capacity for MB was calculated to be 531 mg·g^{-1}, which is higher than most of the previously reported biobased adsorbents such as native biomaterials (NBs),[34,35] nanocellulose (NC),[36−38] and biopolymer-inorganic composites (BICs) (Figure 6c).[34,39−41] On the other hand, our BHA shows slightly lower adsorption capacity than TEMPO-oxidized cellulose nanocrystal CNC (TOCNC) and thiourea-modified carboxymethyl cellulose (TMCC);[36,42] however, the use of hazardous chemicals, i.e., concentric sulfuric acid and thiourea, renders those adsorbents less acceptable for environmental remediation purposes than BHA.

Figure 6d shows the adsorption kinetics of As(III) onto BHA. The adsorption of As(III) increased rapidly in the first 2 h, and the removal of As(III) reached the adsorption equilibrium within 3 h. This high adsorption rate can be attributed to the porous net-like cell structure of BHAs that ensures a fast diffusion As(III). The As(III) adsorption data fitted well to a second-order (eq 3) model (Table 2). Figure 6e shows the adsorption isotherms of As(III) onto BHA. The adsorption isotherm data were fitted well for both Langmuir and Freundlich models (Table 2). The maximum Langmuir adsorption capacity for As(III) was determined to be 217 mg·g^{-1}, which is considered to be a super-high capacity. In Figure 6f, we provide a comparative collection of the present BHA adsorbent versus other pertinent As(III) adsorbents presented in the literature. It is clear in Figure 6f that the BHA is superior to many of the previously reported adsorbents, such as metal−

DOI: 10.1021/acsami.9b15139
ACS Appl. Mater. Interfaces 2019, 11, 46714−46725

organic frameworks (MOFs),[43−45] polymer-miner composites (PMCs),[46,47] modified natural polymers (MNPs),[48−51] and carbon-based materials (CBMs)[52−54] for As(III) sorption.

2.3.3. Desorption and Reusability. The negatively charged carboxylate groups and the free electron doublet of nitrogen on amine groups are known to be responsible for the sorption of MB through an electrostatic attraction mechanism under alkaline conditions. Thus, desorption can be carried out using an acidic solution, where both carboxylate and amine groups will be cationized and the sorption of MB will be reversed. The HCl solution (0.05 M) was found to be an effective eluent for MB desorption, where the adsorbed MB can be completely recovered (>99%). The reusability of the BHA adsorbent was studied by repeating five cycles of the adsorption−desorption process (Figure 7). After the first cycle, the adsorption capacity

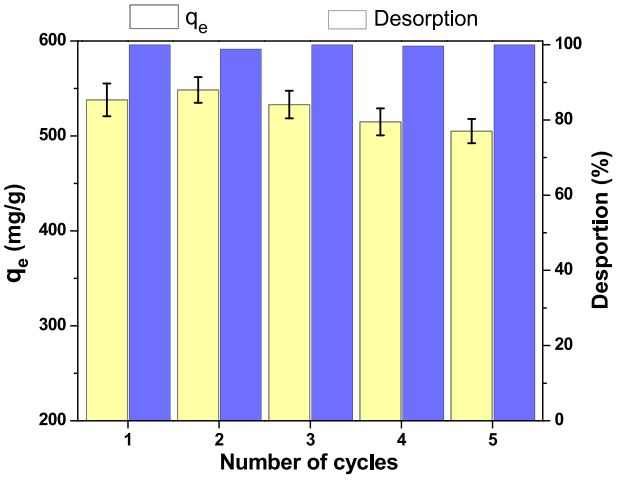

Figure 7. Recycling of the BHA for the removal of MB (pH = 10, C_0 = 200 mg·L^{-1}, T = 25 °C).

was found increased by 2%; this was probably due to the acid treatment activated by some functional groups on BHA for MB adsorption. After the fifth cycle, the BHA still exhibits a high adsorption capacity of 505 mg·g^{-1}. This capacity was still much greater than most of the biobased adsorbents.[34−37,39,41] Thus, the results suggest that this novel BHA can be used as a high-performance reusable adsorbent for the treatment of industrial pollutants.

3. CONCLUSIONS

In brief, a novel and facile method is demonstrated to produce cellulose and chitin composite hydrogel and aerogel. For the first time, the BHH is produced through the electrostatic-force-induced self-assembly of nanocellulose and nanochitin. Lyophilization of BHH yields an ultralight, porous, and high-surface-area BHA adsorbent, which exhibits good adsorption capacities for MB and As(III). Adsorption was favored at high pH values for both MB and As(III). The maximum Langmuir MB adsorption capacity at pH 10 was 531 g·mg^{-1} for this BHA. This high MB uptake can be attributed to the abundant active sites (i.e., −COOH, −NH$_2$) on the surface of BHA. The maximum Langmuir As(III) adsorption capacity at neutral pH was 217 g·mg^{-1}. The BHA was also found to be reusable, as it showed an adsorption capacity of 505 mg·g^{-1} for MB even after five successive adsorption−desorption cycles. This work not only opens a new window for the preparation of hydrogels and aerogels from biopolymer cellulose and chitin but also demonstrates a high-efficiency biobased superadsorbent for water purification.

4. EXPERIMENTAL SECTION

4.1. Materials. Cellulose nanofiber (CNF, 3% aqueous slurry) was obtained from the Process Development Center at the University of Maine. The CNF was produced through a series of mechanical defibril processes of wood pulp. Chitin (originally made from shrimp shell, product # C7170) and TEMPO were purchased from Sigma-Aldrich. Other chemicals such as NaBr, NaClO, NaOH, HCl, NaCl, ethanol, MB solution (1.5 wt %), and sodium arsenite (AsNaO$_2$) were purchased from Fisher Scientific. TOCNF and PDChNF were prepared through TEMPO oxidation and NaOH treatment methods, respectively.[10,25] The detailed processes are illustrated in the Supporting Information (SI).

4.2. Self-Assembly of TOCNF/PDChNF Hydrogel and Aerogel. In a typical self-assembly process, a 10 mL PDChNF suspension was added into a 10 mL TOCNF suspension in a 30 mL beaker followed by shaking the mixture for ∼20s (Figure 2 and Video S1). After the BHH was formed, it was taken out from water using a lab spatula. The volume of BHH was determined by measuring the volume of residue water in the beaker and calculating the difference. To investigate the effect of concentration on the formation of BHH, six different concentrations of TOCNF (10 mL) and PDChNF (10 mL) suspensions (0.01, 0.03, 0.06, 0.10, 0.15, 0.30 wt %) were used to make BHHs. To investigate the effect of PDChNF/TOCNF mass ratio on the formation of BHH, the PDChNF suspension was added to the TOCNF suspension for a given PDChNF/TOCNF mass ratio (3/7, 4/6, 5/5, 6/4, 7/3, 8/2), and the total volume of the mixture suspension was 20 mL. The BHA was produced through quickly freezing the BHH at −196 °C with the liquid nitrogen, followed by freeze-drying (Labconco FreeZone Plus 4.5-Liter) at −80 °C for 2 days. The weight of BHA was determined using a thermos-gravimetric analyzer (SDT Q600 series, TA instrument) to calculate the self-assembly yield using eq 1.

4.3. Characterization. The dimensions (length and diameter) and mass of the cylindrical shaped aerogels were measured using a digital caliper (0.01 mm resolution) and balance (0.1 mg resolution), respectively, to calculate the aerogel density (ρ_a). The porosity of aerogel was calculated as

$$\text{porosity}\ (\%) = \left(1 - \frac{2\rho_a}{\rho_{Ce} + \rho_{Ch}}\right) \times 100\% \quad (4)$$

where ρ_{Ce} and ρ_{Ch} are the bulk densities of cellulose (1500 mg·cm^{-3}) and chitin (1425 mg·cm^{-3}), respectively.

For SEM (JEM-6110 LV, JOEL) characterization, the BHA sample was sputter-coated with 30 nm gold and imaged at a 5 kV accelerating voltage.

The specific surface area and pore size distribution of BHA were measured by N$_2$ adsorption at −196 °C using a gas sorption analyzer (Autosorb iQ, Quantachrome Instruments). Prior to N$_2$ adsorption measurement, aerogel samples were degassed at 110 °C under a vacuum for 2 h. The specific surface area was calculated by the Brunauer−Emmett−Teller (BET) method. Pore size distribution was determined by the Barrett−Joyner−Halenda (BJH) method.

TGA of BHA was performed using a thermos-gravimetric analyzer (SDT Q600 series, TA instrument). Compressed aerogel samples (approximately 6 mg) were heated from 50 to 700 °C at a ramping rate of 10 °C·min^{-1} in a nitrogen (100 mL·min^{-1}) atmosphere. DSC analysis of BHA was performed under N$_2$ at a heating rate of 10 °C·min^{-1} from 30 to 550 °C for aerogel and its precursors using a TA Instrument's Q20 differential scanning calorimeter.

FTIR spectrum of BHA was recorded in the attenuated total reflectance (ATR) mode (PerkinElmer Spectrum Two spectrometer) in the range of 450−4000 cm^{-1} as an average of 10 scans with a 4 cm^{-1} resolution. The spectra were baseline-corrected using Spectrum Quant software through the "data tune-up" function.

DOI: 10.1021/acsami.9b15139
ACS Appl. Mater. Interfaces 2019, 11, 46714−46725

The PZC of BHA was determined using the pH drift method, holding the ionic strength constant with 0.01 M NaCl. Briefly, the solution pH was adjusted from 1 to 13, in intervals of 2, using either NaOH or HCl solutions. The solutions (25 mL) were equilibrated with 6 mg of adsorbent in a shaking water bath (200 rpm) at 25 °C for 24 h.

XPS measurements were conducted with a Thermo Scientific K-Alpha (Kα) XPS system equipped with a monochromatic X-ray source at 1486.6 eV, corresponding to the Al Kα line, with a spot size of 400 μm. BHA samples (~6 mg) were equilibrated with 0.01 M NaCl solutions at various pH values (1, 3, 5, 7, 9, 11, 13). After drying the sample in a gas sorption analyzer degasser system under an argon atmosphere at 120 °C for 1 h, the dried BHA was subjected to XPS analysis.

For comparison purpose, the TGA, DSC, and FTIR experiments were also conducted for TOCNF and PDChNF. To obtain the dried TOCNF and PDChNF materials, TOCNF (0.6 wt %) and PDChNF (0.3 wt %) suspensions were freeze-dried at −80 °C for 2 days.

4.4. Adsorption Experiments. The BHA produced from an optimized condition (PDChNF/TOCNF = 5/5 in weight, concentration of nanofibers = 0.03 wt %) was used for MB and As(III) adsorptions through batch adsorption experiments. Briefly, a 6 mg BHA sample was added into 40 mL adsorbate solutions; the mixture was degassed under vacuum for 2 min, followed by shaking the mixture at 200 rpm with a mechanical shaker for a predefined period of time. The effects of solution pH, contact time, and initial concentration were investigated.

The concentrations of the MB solution before and after adsorption were measured using a UV−vis spectrophotometer (Varian Cary 100 Spectrophotometer) in a wavelength range of 500−800 nm. The adsorption intensity of MB (λ_{max} = 664) was converted to a concentration value using a linear regression curve obtained from the calibration curve over the MB concentration range of 2−10 mg·L^{-1}. Three different calibration curves (Figure S4) were made at acidic (pH 2), neutral (pH 7), and basic (pH 10) conditions, respectively. The concentrations of MB after adsorption were calculated using the corresponding calibration curves. The concentrations of the As(III) solution before and after adsorption were measured using an inductively coupled plasma mass spectrophotometer (ICP-MS) (PerkinElmer SCIEX, ELAN DRC II) with an LOQ of 0.1 μg·L^{-1}. All adsorption experiments were conducted at 25 °C with three replicates, and the initial pH of adsorbate solutions was adjusted using either HCl or NaOH. The adsorption capacity (q) was evaluated using the following equation

$$q = \frac{(C_0 - C_t) \times V}{m} \quad (5)$$

where C_0 (mg·L^{-1}) and C_t (mg·L^{-1}) are the concentrations of adsorbates before and after adsorption, respectively, V (L) is the volume of adsorbate solution, and m (g) is the weight of the dried aerogel.

4.5. Desorption and Reusability. To investigate the reusability of the adsorbents, 6 mg of BHA was added to a 40 mL MB solution (200 mg·L^{-1}, pH = 10) and shaken (200 rpm with a mechanical shaker) at 25 °C for 24 h to achieve saturated adsorption. After adsorption, the BHA was first thoroughly washed with deionized water to remove the residual dye solution. Then, the BHA was immersed in 15 mL of a 0.05 M HCl solution and shaken (200 rpm) at 25 °C for 2 h to strip the adsorbed MB. This desorption process was conducted for three cycles to strip all of the adsorbed MB. The collected MB solution from BHA desorption was diluted 10 times to determine the concentration of desorbed MB, and the desorption efficiency was calculated as eq 6

$$\text{desorption percentage (\%)} = \frac{C_b \times V_b}{q_e \times m} \times 100\% \quad (6)$$

where C_b is the dye concentration after desorption, V_b is the solution volume, q_e is the adsorption capacity at the equilibrium, and m is the mass content of the mass of BHA. The recycled BHA was then rinsed with 150 mL of deionized water and used for the next adsorption cycle. The adsorption and desorption were conducted for five cycles.

■ ASSOCIATED CONTENT

Supporting Information

The Supporting Information is available free of charge at https://pubs.acs.org/doi/10.1021/acsami.9b15139.

Self-assembly process (MP4)

TOCNF and PDChNF preparation procedures; characterization results of TOCNF and PDChNF; comparison of FTIR spectra of BHA, TOCNF, and PDChNF; digital image of BHA handled by tweezers (PDF)

■ AUTHOR INFORMATION

Corresponding Authors

*E-mail: xz210@msstate.edu (X.Z.).

*E-mail: e.hassan@msstate.edu (E.B.H.).

ORCID

Xuefeng Zhang: 0000-0003-1654-3969

Islam Elsayed: 0000-0002-5148-3693

Chanaka Navarathna: 0000-0001-7910-2787

Gregory T. Schueneman: 0000-0002-6390-5240

EI Barbary Hassan: 0000-0002-7980-9800

Notes

The authors declare no competing financial interest.

■ ACKNOWLEDGMENTS

This work was financially supported by USDA Forest Products Laboratory through grant G00002749. The authors thank Dr. Felio Perez from the University of Memphis for his assistance in XPS experiments. This manuscript is publication #SB954 of the Sustainable Bioproducts, Mississippi State University.

■ REFERENCES

(1) Singh, R.; Singh, S.; Parihar, P.; Singh, V. P.; Prasad, S. M. Arsenic Contamination, Consequences and Remediation Techniques: A Review. *Ecotoxicol. Environ. Saf.* **2015**, *112*, 247−270.

(2) Bissen, M.; Frimmel, F. H. Arsenic — a Review. Part II: Oxidation of Arsenic and Its Removal in Water Treatment. *Acta Hydrochim. Hydrobiol.* **2003**, *31*, 97−107.

(3) Li, L.; Lan Liu, X.; Yun Geng, H.; Hu, B.; Wu Song, G.; Shun Xu, Z. A MOF/Graphite Oxide Hybrid (MOF: HKUST-1) Material for the Adsorption of Methylene Blue from Aqueous Solution. *J. Mater. Chem. A* **2013**, *1*, 10292−10299.

(4) Ponnusami, V.; Vikram, S.; Srivastava, S. N. Guava (Psidium Guajava) Leaf Powder: Novel Adsorbent for Removal of Methylene Blue from Aqueous Solutions. *J. Hazard. Mater.* **2008**, *152*, 276−286.

(5) Hu, X.-S.; Liang, R.; Sun, G. Super-Adsorbent Hydrogel for Removal of Methylene Blue Dye from Aqueous Solution. *J. Mater. Chem. A* **2018**, *6*, 17612−17624.

(6) Mao, J.; Ge, M.; Huang, J.; Lai, Y.; Lin, C.; Zhang, K.; Meng, K.; Tang, Y. Constructing Multifunctional MOF@rGO Hydro-/Aerogels by the Self-Assembly Process for Customized Water Remediation. *J. Mater. Chem. A* **2017**, *5*, 11873−11881.

(7) Zubyk, H.; Mykhailiv, O.; Papathanassiou, A. N.; Sulikowski, B.; Zambrzycka-Szelewa, E.; Bratychak, M.; Plonska-Brzezinska, M. E. A Phenol-Formaldehyde Polymeric Network to Generate Organic Aerogels: Synthesis, Physicochemical Characteristics and Potential Applications. *J. Mater. Chem. A* **2018**, *6*, 845−852.

(8) Zhao, D.; Tian, Y.; Jing, X.; Lu, Y.; Zhu, G. PAF-1@cellulose Nanofibril Composite Aerogel for Highly-Efficient Removal of Bisphenol A. *J. Mater. Chem. A* **2019**, *7*, 157−164.

(9) Xiong, Y.; Wang, C.; Wang, H.; Yao, Q.; Fan, B.; Chen, Y.; Sun, Q.; Jin, C.; Xu, X. A 3D Titanate Aerogel with Cellulose as the

DOI: 10.1021/acsami.9b15139
ACS Appl. Mater. Interfaces 2019, 11, 46714−46725

Adsorption-Aggregator for Highly Efficient Water Purification. *J. Mater. Chem. A* **2017**, *5*, 5813−5819.
(10) Liu, L.; Bai, L.; Tripathi, A.; Yu, J.; Wang, Z.; Borghei, M.; Fan, Y.; Rojas, O. J. High Axial Ratio Nanochitins for Ultrastrong and Shape-Recoverable Hydrogels and Cryogels via Ice Templating. *ACS Nano* **2019**, *13*, 2927−2935.
(11) Lavoine, N.; Bergstrom, L. Nanocellulose-Based Foams and Aerogels: Processing, Properties, and Applications. *J. Mater. Chem. A* **2017**, *5*, 16105−16117.
(12) Jiang, F.; Hsieh, Y.-L. Super Water Absorbing and Shape Memory Nanocellulose Aerogels from TEMPO-Oxidized Cellulose Nanofibrils via Cyclic Freezing−Thawing. *J. Mater. Chem. A* **2014**, *2*, 350−359.
(13) Shen, X.; Shamshina, J. L.; Berton, P.; Gurau, G.; Rogers, R D. Hydrogels Based on Cellulose and Chitin: Fabrication, Properties, and Applications. *Green Chem.* **2016**, *18*, 53−75.
(14) Kono, H.; Fujita, S. Biodegradable Superabsorbent Hydrogels Derived from Cellulose by Esterification Crosslinking with 1,2,3,4-Butanetetracarboxylic Dianhydride. *Carbohydr. Polym.* **2012**, *87*, 2582−2588.
(15) Fu, J.; Yang, F.; Guo, Z. The Chitosan Hydrogels: From Structure to Function. *New J. Chem.* **2018**, *42*, 17162−17180.
(16) Nascimento, D. M.; Nunes, Y. L.; Figueiredo, M. C. B.; Azeredo, H. M. C.; de Aouada, F. A.; Feitosa, J. P. A.; Rosa, M. F.; Dufresne, A. Nanocellulose Nanocomposite Hydrogels: Technological and Environmental Issues. *Green Chem.* **2018**, *20*, 2428−2448.
(17) De France, K. J.; Hoare, T.; Cranston, E. D. Review of Hydrogels and Aerogels Containing Nanocellulose. *Chem. Mater.* **2017**, *29*, 4609−4631.
(18) Sun, X.; Peng, B.; Ji, Y.; Chen, J.; Li, D. Chitosan(Chitin)/Cellulose Composite Biosorbents Prepared Using Ionic Liquid for Heavy Metal Ions Adsorption. *AIChE J.* **2009**, *55*, 2062−2069.
(19) Wu, J.; Liang, S.; Dai, H.; Zhang, X.; Yu, X.; Cai, Y.; Zhang, L.; Wen, N.; Jiang, B.; Xu, J. Structure and Properties of Cellulose/Chitin Blended Hydrogel Membranes Fabricated via a Solution Pre-Gelation Technique. *Carbohydr. Polym.* **2010**, *79*, 677−684.
(20) Tang, H.; Chen, H.; Duan, B.; Lu, A.; Zhang, L. Swelling Behaviors of Superabsorbent Chitin/Carboxymethylcellulose Hydrogels. *J. Mater. Sci.* **2014**, *49*, 2235−2242.
(21) Liang, S.; Zhang, L.; Xu, J. Morphology and Permeability of Cellulose/Chitin Blend Membranes. *J. Membr. Sci.* **2007**, *287*, 19−28.
(22) Yamazaki, S.; Takegawa, A.; Kaneko, Y.; Kadokawa, J.; Yamagata, M.; Ishikawa, M. Performance of Electric Double-Layer Capacitor with Acidic Cellulose−Chitin Hybrid Gel Electrolyte. *J. Electrochem. Soc.* **2010**, *157*, A203−A208.
(23) Zhou, D.; Zhang, L.; Zhou, J.; Guo, S. Cellulose/Chitin Beads for Adsorption of Heavy Metals in Aqueous Solution. *Water Res.* **2004**, *38*, 2643−2650.
(24) Gao, K.; Guo, Y.; Niu, Q.; Fang, H.; Zhang, L.; Zhang, Y.; Wang, L.; Zhou, L. Effects of Chitin Nanofibers on the Microstructure and Properties of Cellulose Nanofibers/Chitin Nanofibers Composite Aerogels. *Cellulose* **2018**, *25*, 4591−4602.
(25) Jiang, F.; Hsieh, Y.-L. Chemically and Mechanically Isolated Nanocellulose and Their Self-Assembled Structures. *Carbohydr. Polym.* **2013**, *95*, 32−40.
(26) Liu, L.; Wang, R.; Yu, J.; Jiang, J.; Zheng, K.; Hu, L.; Wang, Z.; Fan, Y. Robust Self-Standing Chitin Nanofiber/Nanowhisker Hydrogels with Designed Surface Charges and Ultralow Mass Content via Gas Phase Coagulation. *Biomacromolecules* **2016**, *17*, 3773−3781.
(27) Jiang, F.; Hsieh, Y.-L. Self-Assembling of TEMPO Oxidized Cellulose Nanofibrils As Affected by Protonation of Surface Carboxyls and Drying Methods. *ACS Sustainable Chem. Eng.* **2016**, *4*, 1041−1049.
(28) Dewage, N. B.; Fowler, R. E.; Pittman, C. U.; Mohan, D.; Mlsna, T. Lead (Pb2+) Sorptive Removal Using Chitosan-Modified Biochar: Batch and Fixed-Bed Studies. *RSC Adv.* **2018**, *8*, 25368−25377.
(29) da Silva Perez, D.; Montanari, S.; Vignon, M. R. TEMPO-Mediated Oxidation of Cellulose III. *Biomacromolecules* **2003**, *4*, 1417−1425.
(30) Mohammed, M. A.; Syeda, J. T. M.; Wasan, K. M.; Wasan, E. K. An Overview of Chitosan Nanoparticles and Its Application in Non-Parenteral Drug Delivery. *Pharmaceutics* **2017**, *9*, 53.
(31) Impert, O.; Katafias, A.; Kita, P.; Mills, A.; Pietkiewicz-Graczyk, A.; Wrzeszcz, G. Kinetics and Mechanism of a Fast Leuco-Methylene Blue Oxidation by Copper(II)−Halide Species in Acidic Aqueous Media. *Dalton Trans.* **2003**, 348−353.
(32) Sun, X.; Doner, H. E. An Investigation of Arsenate and Arsenite Bonding Structures on Goethite by FTIR. *Soil Sci.* **1996**, *161*, 865.
(33) Wang, N.; Ouyang, X.-K.; Yang, L.-Y.; Omer, A. M. Fabrication of a Magnetic Cellulose Nanocrystal/Metal−Organic Framework Composite for Removal of Pb(II) from Water. *ACS Sustainable Chem. Eng.* **2017**, *5*, 10447−10458.
(34) Cao, Y.-L.; Pan, Z.-H.; Shi, Q.-X.; Yu, J.-Y. Modification of Chitin with High Adsorption Capacity for Methylene Blue Removal. *Int. J. Biol. Macromol.* **2018**, *114*, 392−399.
(35) Liu, L.; Fan, S.; Li, Y. Removal Behavior of Methylene Blue from Aqueous Solution by Tea Waste: Kinetics, Isotherms and Mechanism. *Int. J. Environ. Res. Public Health* **2018**, *15*, No. 1321.
(36) Batmaz, R.; Mohammed, N.; Zaman, M.; Minhas, G.; Berry, R. M.; Tam, K. C. Cellulose Nanocrystals as Promising Adsorbents for the Removal of Cationic Dyes. *Cellulose* **2014**, *21*, 1655−1665.
(37) Chan, C. H.; Chia, C. H.; Zakaria, S.; Sajab, M. S.; Chin, S. X. Cellulose Nanofibrils: A Rapid Adsorbent for the Removal of Methylene Blue. *RSC Adv.* **2015**, *5*, 18204−18212.
(38) Yang, X.; Liu, H.; Han, F.; Jiang, S.; Liu, L.; Xia, Z. Fabrication of Cellulose Nanocrystal from Carex Meyeriana Kunth and Its Application in the Adsorption of Methylene Blue. *Carbohydr. Polym.* **2017**, *175*, 464−472.
(39) Mohammed, N.; Grishkewich, N.; Berry, R. M.; Tam, K. C. Cellulose Nanocrystal−Alginate Hydrogel Beads as Novel Adsorbents for Organic Dyes in Aqueous Solutions. *Cellulose* **2015**, *22*, 3725−3738.
(40) Wei, X.; Huang, T.; Yang, J.; Zhang, N.; Wang, Y.; Zhou, Z. Green Synthesis of Hybrid Graphene Oxide/Microcrystalline Cellulose Aerogels and Their Use as Superabsorbents. *J. Hazard. Mater.* **2017**, *335*, 28−38.
(41) Auta, M.; Hameed, B. H. Chitosan−Clay Composite as Highly Effective and Low-Cost Adsorbent for Batch and Fixed-Bed Adsorption of Methylene Blue. *Chem. Eng. J.* **2014**, *237*, 352−361.
(42) Pan, Y.; Shi, X.; Cai, P.; Guo, T.; Tong, Z.; Xiao, H. Dye Removal from Single and Binary Systems Using Gel-like Bioadsorbent Based on Functional-Modified Cellulose. *Cellulose* **2018**, *25*, 2559−2575.
(43) Yu, X.; Tong, S.; Ge, M.; Zuo, J.; Cao, C.; Song, W. One-Step Synthesis of Magnetic Composites of Cellulose@iron Oxide Nanoparticles for Arsenic Removal. *J. Mater. Chem. A* **2013**, *1*, 959−965.
(44) Kwon, O.-H.; Kim, J.-O.; Cho, D.-W.; Kumar, R.; Baek, S. H.; Kurade, M. B.; Jeon, B.-H. Adsorption of As(III), As(V) and Cu(II) on Zirconium Oxide Immobilized Alginate Beads in Aqueous Phase. *Chemosphere* **2016**, *160*, 126−133.
(45) Zhou, S.; Wang, D.; Sun, H.; Chen, J.; Wu, S.; Na, P. Synthesis, Characterization, and Adsorptive Properties of Magnetic Cellulose Nanocomposites for Arsenic Removal. *Water. Air. Soil Pollut.* **2014**, *225*, 1945.
(46) Hokkanen, S.; Doshi, B.; Srivastava, V.; Puro, L.; Koivula, R. Arsenic (III) Removal from Water by Hydroxyapatite-Bentonite Clay-Nanocrystalline Cellulose. *Environ. Prog. Sustainable Energy 38* 13147. DOI: 10.1002/ep.13147.
(47) Saleh, T. A.; Sarı, A.; Tuzen, M. Chitosan-Modified Vermiculite for As(III) Adsorption from Aqueous Solution: Equilibrium, Thermodynamic and Kinetic Studies. *J. Mol. Liq.* **2016**, *219*, 937−945.
(48) Yu, X.; Tong, S.; Ge, M.; Wu, L.; Zuo, J.; Cao, C.; Song, W. Synthesis and Characterization of Multi-Amino-Functionalized

DOI: 10.1021/acsami.9b15139
ACS Appl. Mater. Interfaces 2019, 11, 46714−46725

Cellulose for Arsenic Adsorption. *Carbohydr. Polym.* **2013**, *92*, 380−387.
(49) Hanh, T. T.; Huy, H. T.; Hien, N. Q. Pre-Irradiation Grafting of Acrylonitrile onto Chitin for Adsorption of Arsenic in Water. *Radiat. Phys. Chem.* **2015**, *106*, 235−241.
(50) Yang, R.; Su, Y.; Aubrecht, K. B.; Wang, X.; Ma, H.; Grubbs, R. B.; Hsiao, B. S.; Chu, B. Thiol-Functionalized Chitin Nanofibers for As (III) Adsorption. *Polymer* **2015**, *60*, 9−17.
(51) Mcafee, B. J.; Gould, W. D.; Nadeau, J. C.; da Costa, A. C. A. Biosorption of Metal Ions Using Chitosan, Chitin, and Biomass of Rhizopus Oryzae. *Sep. Sci. Technol.* **2001**, *36*, 3207−3222.
(52) Navarathna, C. M.; Karunanayake, A. G.; Gunatilake, S. R.; Pittman, C. U.; Perez, F.; Mohan, D.; Mlsna, T. Removal of Arsenic(III) from Water Using Magnetite Precipitated onto Douglas Fir Biochar. *J. Environ. Manage.* **2019**, *250*, No. 109429.
(53) Yoon, Y.; Park, W. K.; Hwang, T.-M.; Yoon, D. H.; Yang, W. S.; Kang, J.-W. Comparative Evaluation of Magnetite−Graphene Oxide and Magnetite-Reduced Graphene Oxide Composite for As(III) and As(V) Removal. *J. Hazard. Mater.* **2016**, *304*, 196−204.
(54) Eguez, H. E.; Cho, E. H. Adsorption of Arsenic on Activated Charcoal. *JOM* **1987**, *39*, 38−41.

DOI: 10.1021/acsami.9b15139
ACS Appl. Mater. Interfaces 2019, 11, 46714−46725